Vehmas, Joni; Järveläinen, Jan; Nguyen, Sinh Le Hong; Naderpour, Reza; Haneda, Katsuyuki

Millimeter-wave channel characterization at Helsinki Airport in the 15, 28, and 60 GHz bands

Published in:
2016 IEEE 84th Vehicular Technology Conference, VTC Fall 2016 - Proceedings

DOI:
10.1109/VTCFall.2016.7881086

Published: 01/01/2017

Document Version
Peer reviewed version

Millimeter-Wave Channel Characterization at Helsinki Airport in the 15, 28, and 60 GHz Bands

Joni Vehmas, Jan Järveläinen, Sinh Le Hong Nguyen, Reza Naderpour, and Katsuyuki Haneda
Aalto University, School of Electrical Engineering, Department of Radio Science and Engineering, Espoo, Finland
Email: joni.vehmas@aalto.fi

***Abstract*—Airport terminal is one of the indoor scenarios envisioned for the fifth generation millimeter-wave deployment. However, relatively little research effort has been devoted to its characterization at millimeter waves this far. In this paper, we characterize the propagation channel at Helsinki Airport in the 15, 28, and 60 GHz bands by means of directional wideband channel sounding. The radio environment is analyzed by studying the specular propagation paths, specular and diffuse power contributions, polarization, and the delay and angular spreads. Many of the studied metrics show relatively few differences for the three frequency bands though some slight trends can be observed.**

I. Introduction

Millimeter-wave (mm-wave) communications will be a vital part of the forthcoming fifth generation (5G) wireless communication systems in enabling very high throughput for hotspots and backhaul links. Although mm-wave channel measurements have been reported widely [1], the availability of results in many of the scenarios envisioned for mm-wave 5G deployment, such as shopping malls and airports [2], [3], is poor. For instance, airport terminals have been studied only in a few papers, such as in [4]. Moreover, the frequency dependency of propagation properties in such scenarios is largely unknown, although a few works report the influence of frequency on the path loss and delay spread [5], [6].

In this paper, we present results from channel sounding in an airport terminal at 15, 28, and 60 GHz. The goal of the paper is to characterize the radio environment in the three frequency bands using multiple metrics such as specular and diffuse power spectra and decay factors, cross polarization ratios (XPRs), and delay, azimuth, and elevation spreads.

The paper is organized as follows: Section II describes the channel sounding setup and the scenario as well as preliminary measurement results. In Section III, the propagation path detection based on the measurement results is elaborated. Section IV includes more in-depth analysis of the measurement results and characterization of the radio channel. Finally, Section V concludes the paper.

II. Radio Channel Sounding

A. Mm-Wave Channel Sounder

The mm-wave channel sounder is based on a vector network analyzer (VNA), as seen from Fig. 1. At 28 and 60 GHz, a Rohde & Schwartz SMP 22 signal generator and frequency up and down converters (manufactured by Sivers IMA) are used to achieve the wanted radio frequency (RF)

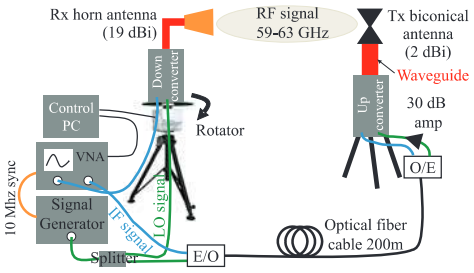

Fig. 1. Schematic of the 60 GHz channel sounder.

TABLE I
Summary of channel sounding system parameters.

Description	15 GHz	28 GHz	60 GHz
IF frequency [GHz]	N/A	1-4	1-5
LO frequency [GHz]	N/A	13	14.5
RF frequency [GHz]	14-16	27-30	59-63
IF bandwidth [kHz]	5	5	1
Transmit power [dBm]	17	7	17
No. of frequency steps	10001	10001	2001/5001

by mixing the local oscillator (LO) signal from the generator with the intermediate frequency (IF) signal from an Agilent Technologies E8363A VNA. In the 15-GHz sounder, the VNA is connected directly to the antennas. Both the transmitting (Tx) and receiving (Rx) antennas have close to identical characteristics at all the studied frequencies. Co-polarized (co-pol) and cross-polarized (x-pol) channels are measured using vertical to vertical polarized antennas and vertical to horizontal polarized antennas, respectively. On the Tx side, 2-dBi omnidirectional biconical antennas with elevation HPBWs of more than 60° are used for both polarizations. For the co-pol case, the Rx antennas are directive H-plane sectoral horn antennas with gains of 19 dBi and 10° and 40° half-power beamwidths (HPBWs) in the azimuth and elevation domains, respectively. In x-pol measurements, the horn antennas have similar radiation patterns as the co-pol antennas when rotated by 90°. To capture the directional properties of the channel, the Rx antenna is rotated in the azimuth plane from 20° to 160° with 5° steps, and in each antenna pointing angle a channel transfer function (CTF) is recorded. The azimuth sweeps are conducted with the elevation angle set to either 0° or −20°. Table I summarizes the channel sounding setup for the three frequency bands.

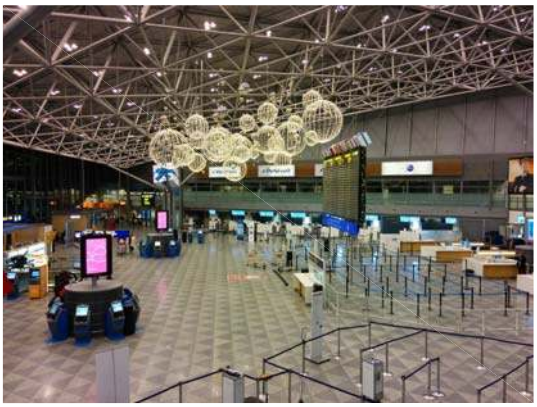

Fig. 2. Terminal hall seen from the Rx antenna.

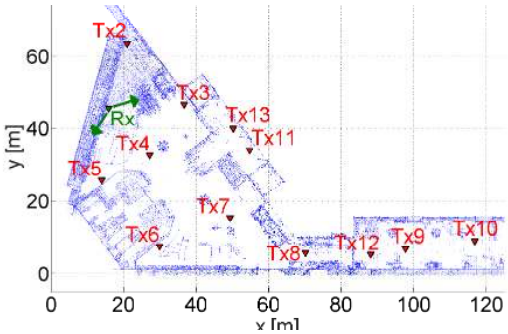

Fig. 3. Measurement floor plan depicted on top of 3D point cloud model. The Rx azimuthal scan range (20°–160°) is shown with green arrows (upper arrow corresponding to 20°).

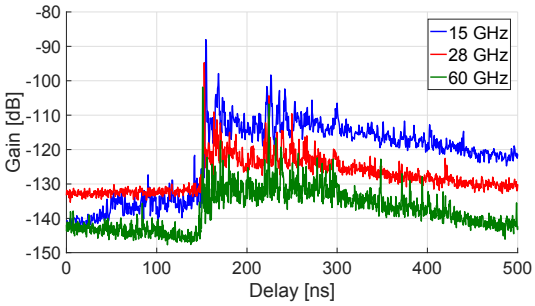

Fig. 4. Measured PDPs for Tx7 with 0° antenna elevation angle.

B. Measurement Scenario

Channel sounding was conducted in the three mm-wave bands in Terminal 2 of Helsinki Airport, shown in Fig. 2. To avoid human blockage effects, the measurements were conducted in the evening and at night due to which the area was almost devoid of people. The 15 and 28 GHz measurements were conducted during Christmas time in the presence of some Christmas decorations, which were absent during the later 60 GHz measurements.

Altogether 12 Tx locations and a single Rx location were considered in the measurements, as presented in Fig. 3. Five of the Tx locations correspond to LOS links (Tx3–Tx7) and the rest correspond to NLOS links. The link distance varies between 18.8 m and 107.2 m. All the Tx locations are on the main terminal level (antenna height 1.58 m) except for Tx11 and Tx13, which are on a lower, ground level (antenna height -2.62 m relative to the main terminal level), whereas Rx is located on the loft-like higher level overlooking the terminal hall (antenna height 5.68 m relative to the main terminal level). The Tx locations 2–10 were measured for all the studied frequencies while Tx11 was measured only at 15 and 60 GHz, Tx12 was measured only at 28 GHz and 60 GHz, and Tx13 was measured only at 28 GHz. Tx1 was a test measurement which is not considered in this paper.

C. Data Processing and Results

In order to conduct analysis based on the measurements, we first derive the power angular delay profile (PADP) and the power delay profile (PDP) for each link separately for the two antenna elevation angles starting from the measured CTF for different antenna azimuth angles and polarizations. The azimuth-angular-dependent CTFs are written as $\tilde{H}_c(l,m)$ and $\tilde{H}_x(l,m)$, where l and m are used to denote the frequency and azimuth bins, respectively, while c and x denote the co- and cross-polarizations. An angular-dependent channel impulse response (CIR) h is derived as the inverse fast Fourier transform of each column of $\tilde{H} = \tilde{H}_c + \tilde{H}_x$ with a rectangular window. The PADP can be then derived as $PADP(k,m) = H(k,m) \otimes (H(k,m))^*$ where $\otimes$ and $*$ denote element-wise multiplication and the conjugate operation, respectively and k denotes the delay bins. Consequently, the PDP can be calculated as the ensemble average of the CIRs for the azimuth pointing angles [7]. As an example, PDPs for Tx7 at 15, 28, and 60 GHz with 0° antenna elevation angle are presented in Fig. 4. The three frequencies share a similar shape of the PDP, but have quite different noise levels with the 28-GHz measurements providing notably poorer dynamic range compared to 15 and 60 GHz.

III. Propagation Path Detection

A. Peak detection method

In order to further study the radio channel and particularly to resolve the direction of specular reflections (both in azimuth and elevation), peak detection is used to detect specular paths from PDPs. The detection of the specular propagation paths for each link is done in three parts. First, the propagation paths are detected from the co-pol PDP as local maxima which exceed a certain threshold. This threshold is defined as a sum of a sliding average of the PDP for the near-by delay bins and a certain constant in order to prevent the detection of minor small-scale variations in the PDPs as peaks. For this calculation, a combined PDP, that is, a PDP which is an average of the PDPs for the two elevation angles, is used. Finally, the azimuth direction with the maximum amplitude corresponding to this delay is found from the PADP.

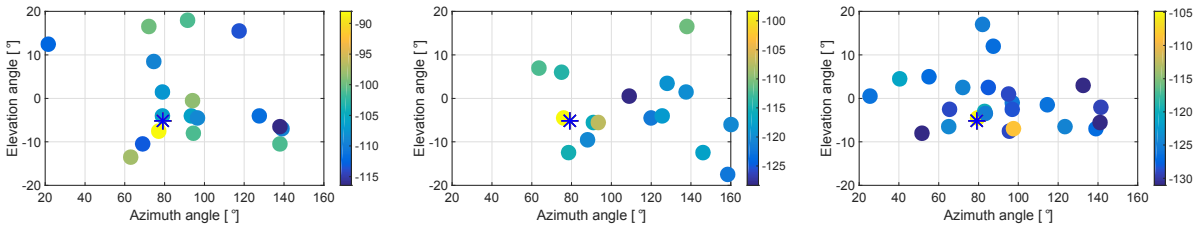

Fig. 5. Detected specular paths and their amplitudes in dB for (a) 15 GHz, (b) 28 GHz, and (c) 60 GHz for Tx7. The symbol $*$ shows the line-of-sight direction calculated based on the Rx and Tx locations.

Second, a finer peak search around the acquired delay bin value is conducted in time domain separately for each elevation angle (-20° and 0°). The two elevation angles are treated here separately in order to take into account the possible small difference in the delay for a given multipath component for different Rx elevation angles. Similar to the path detection method presented in [7], [8], the exact delay for each peak is determined by interpolating over the two neighboring delay bins of the PADP using a peak-normalized gain pattern of the sinc function. Next, based on this interpolation a gain correction term is applied to all the channel impulse responses (both co-pol and x-pol) corresponding to this delay bin. The delay of the multipath component is considered as the mean of the two acquired delay values.

Third, a similar fine peak search is conducted simultaneously for both the azimuth and elevation angles. This is achieved by considering a set of six measured angular bins near the observed local maximum. To be precise, we consider the azimuth–elevation angle pairs (ϕ_{max} - 5°, -20°), (ϕ_{max}, -20°), (ϕ_{max} + 5°, -20°), (ϕ_{max} - 5°, 0°), (ϕ_{max}, 0°), and (ϕ_{max} + 5°, 0°) where ϕ_{max} corresponds to the azimuth angle of the given specular propagation path according to the earlier rough peak search and (ϕ_{max}, 0°) serves as a reference point to which all the other amplitudes are normalized. By fitting this set of five points with given amplitude, azimuth and elevation angles to the normalized 3D gain pattern of the Rx antenna in the least squares sense, we can get an estimate for the azimuth and elevation angles of each multipath, and the needed correction in the peak amplitudes. Finally, the combined antenna gain (21 dB) is subtracted from the co- and x-pol peaks.

In summary, the end result of the peak detection process is a set of corrected specular peaks (both co-pol and x-pol) with delay, azimuth angle, and elevation angle values which are no longer limited to the discrete delay, azimuth, and elevation bin values provided by the measurement.

B. Results

As an example of the peak detection, we will consider the Tx location 7 (LOS). The azimuth and elevation angles for the detected multipaths as well as their amplitudes for the studied frequencies are illustrated in Fig. 5. Only the specular paths which fall within a 30 dB dynamic range are shown. The strongest path is found in all cases near the theoretical LOS direction denoted as $*$ in the figure. However, the other detected paths are quite different depending on the frequency, which is perhaps due to the fact that the environment contains few large smooth surfaces, especially at the same height level as the Rx and Tx. Notably, reflections occur not only from the walls and floor but also from the ceiling structure as evidenced by the positive elevation angles.

IV. Spatio-Temporal Radio Channel Characterization

A. Specular Power Ratio

Knowing the detected specular paths, we can define a ratio between the specular power and the total power $r_{spec} = P_{spec}/P_{tot}$, where P_{spec} is the sum of the power of the detected specular paths and P_{tot} is the sum over the PDP amplitudes for those indices which are above the noise level. The power ratios for the different frequencies and links are shown in Fig. 6, which illustrates how the ratio of the specular power decreases as a function of link distance. In general, the NLOS links have lower r_{spec} compared to LOS links due to the absence of the direct path and a smaller number of specular paths. Although the specular power ratio does not show strong frequency dependency, r_{spec} does seem to increase slightly with higher frequency.

B. Specular Power Decay

In order to study the power decay characteristics of the environment for the specular propagation paths, we will consider the following model excluding the LOS [7]

$$\hat{a}_l = P_0 \exp(-\tau/\beta_0)\xi. \quad (1)$$

Here, P_0 is the initial pathloss, τ is the delay, β_0 is a power decay factor, and ξ is a normal random variable in dB defined according to $10\log_{10}\xi \sim \mathcal{N}(0, \sigma_s^2)$, where σ_s is the standard deviation of the shadow fading. The parameters of the model for each frequency are estimated by, first, performing a linear fit to the detected propagation path amplitudes excluding the LOS paths in the delay domain. For large delays, the peaks with low amplitudes relative to the mean amplitude are no longer detected due to the proximity of the noise floor and therefore only the peaks with large amplitudes can be taken into account which in turn leads to overestimation of the decay factor. Also, the peaks at high delays may no longer follow the simple linear decay model. For these reasons, we set a

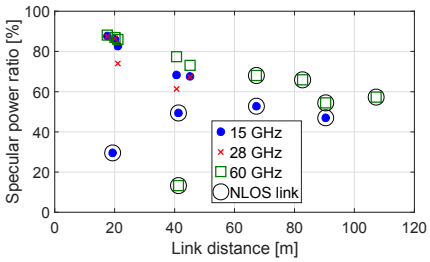

Fig. 6. Specular power ratios at 15, 28, and 60 GHz.

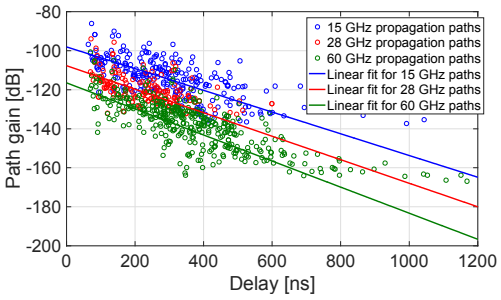

Fig. 7. Specular paths in delay domain. All detected paths excluding the LOS paths are plotted. The solid lines represent the linear fits corresponding to Eq. 1 for each frequency with model parameters given in Table II.

delay limit after which the peaks are no longer taken into account in the fitting. This delay limit is defined for 15 and 60 GHz so that there exists a 14 dB difference between the linear fit at the delay limit and the weakest observed peak. Due to the more limited dynamic and delay ranges in the 28 GHz measurements, a smaller threshold of 10 dB was used at that frequency. Finally, the standard deviation is evaluated by calculating the maximum likelihood estimate for the difference between the detected peak values and the linear fit.

The specular paths for all links and frequencies along with linear fits illustrating the mean decay are shown in Fig. 7. The model parameters are given in Table II. It should be noted that the due to the limited number of detected paths at 28 GHz (owing to the limited dynamic range in the measurements), the uncertainty in the 28 GHz results is higher compared to the 15 and 60 GHz results. Nevertheless, we can observe that the decay factor β_0 decreases with frequency which corresponds to increasing power decay though the values are relatively close to each other at all the studied frequencies.

C. Diffuse Power Decay

The diffuse power is modeled with an exponentially decaying spectrum [7]

$$P_{\text{diff}}(\tau) = \begin{cases} P_n & (\tau < \tau_0) \\ P_d & (\tau = \tau_0), \\ \max\{P_n, P_d \exp(-\tau/\beta_d)\} & (\tau > \tau_0) \end{cases} \quad (2)$$

where P_n is the noise power, τ_0 is the delay of the first path, P_d is the maximum diffuse power, and β_d is the diffuse power

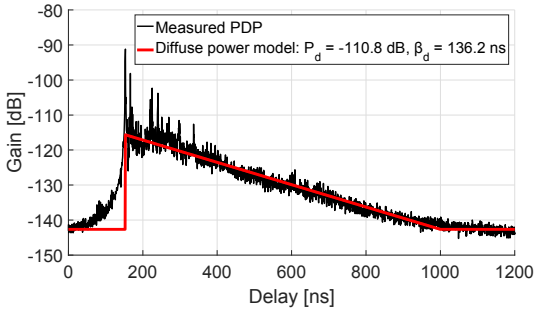

Fig. 8. Measured PDP and diffuse power decay model for Tx7 at 15 GHz.

TABLE II
MODEL PARAMETERS FOR SPECULAR AND DIFFUSE POWER SPECTRUM.

	$\overline{P}_0$ [dB]	$\overline{\beta}_0$ [ns]	σ_s [dB]	$\overline{P}_d$ [dB]	$\overline{\beta}_d$ [ns]
15 GHz	-98.1	78.0	7.2	-110.8	138.9
28 GHz	-107.7	72.1	6.5	N/A	N/A
60 GHz	-116.5	65.0	8.4	-131.8	136.6

decay factor. The model parameters are derived by minimizing the mean square error for each link. An example of this fitting procedure is shown in Fig. 8, where the measured PDP along with the fitted diffuse decay model is presented for Tx7 at 15 GHz. The mean diffuse power parameters are shown in Table II, which emphasizes that no clear frequency dependency can be found for the diffuse decay factor. The difference in P_d between 15 and 60 GHz is more than 20 dB, of which around 12 dB is due to the difference in free-space path loss. The remaining part of roughly 9 dB comes from the relatively stronger diffuse power at lower frequencies. The stronger diffuse power at 15 GHz also explains the lower specular power ratio presented in Sec. IV-A. Moreover, it should be noted that the diffuse power decay factors are significantly larger than the specular power decay factors, implying that diffuse power decays slower than specular power. While in the earlier specular path analysis the antennas were de-embedded, that is, the effect of the antenna patterns to the channel was eliminated, such a de-embedding was not done for diffuse power. This fact should be taken into account when comparing the specular and diffuse model values of Table II, especially the power values.

D. Cross-Polarization Ratio

For each detected path whose x-pol path amplitude is above the noise level, the XPR is calculated simply as the ratio between the co-pol and x-pol path powers. The XPR was not derived for 28 GHz due to the low number of identified x-pol paths. The resulting cumulative distribution functions (CDFs) for 15 and 60 GHz are shown in Fig. 9, which shows almost identical XPR distributions with median values of 19.5 and 19.7 dB, respectively. These results are well in line with previous mm-wave XPR results, reported in, e.g., [9], [10].

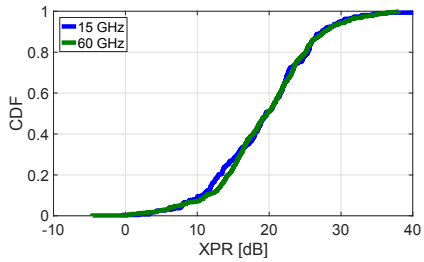

Fig. 9. XPR distribution for 15 and 60 GHz.

TABLE III
MEAN LARGE SCALE PARAMETERS.

	Frequency band	Delay spread [ns]	Azimuth spread [°]	Elevation spread [°]
LOS	**15 GHz**	42.6	19.5	7.0
	28 GHz	34.4	19.6	9.4
	60 GHz	38.7	17.6	5.6
NLOS	**15 GHz**	65.8	30.3	8.4
	28 GHz	N/A	N/A	N/A
	60 GHz	57.1	29.7	9.3

E. Large-Scale Parameters

As was shown in Section IV-A, the radio channel is in most cases dominated by specular reflections. Tx locations 11 and 13, which are located on the lower level, serve as the biggest exceptions to this rule as they are strongly dominated by diffuse scattering and are therefore excluded from the following analysis. For the rest of the links, we calculate the delay, azimuth, and elevation spreads based on the detected specular peaks using the well-established formulas [11]. However, only the propagation paths which fit within the 30 dB dynamic range are considered in the calculation. Furthermore, any links which do not provide 30 dB dynamic range are neglected altogether (namely, 28 GHz NLOS links).

The mean delay, azimuth, and elevation spreads can be seen in Table III. The reported mean parameters are fairly close to each other at different frequencies. Moreover, the values for the delay spread are quite similar to the ones presented in [4] for 28 GHz measurements at Incheon International Airport. The parameters were also studied as functions of the link distance. While no discernible trend was observed in the delay spreads for LOS links, NLOS delay spread was observed to decrease with link distance at all frequencies. This may be partly explained by the fact that the farthest NLOS Tx locations are within the same corridor which serves as a directive medium for these links. The azimuth spread is fairly constant for the NLOS links, but exhibits a slightly decreasing trend for the LOS links. As can be expected based on the differing heights of the antennas, the elevation spread decreases with increasing link distance for both LOS and NLOS links.

V. CONCLUSIONS

In this paper, the radio channel of an airport terminal was characterized in the 15, 28, and 60 GHz bands. Based on directional wideband channel sounding at Helsinki Airport and a propagation path detection algorithm, specular propagation paths were identified and their delay and azimuth and elevation angles were resolved. Based on the detected paths, the properties of the radio channel at the different frequencies were studied in terms of specular power ratio, specular and diffuse power decay, XPR, and delay, azimuth, and elevation spreads. The result shows that differences between the frequency bands are mostly minor though some slight trends can still be observed. For example, the highest specular power ratio and the lowest diffuse power level is achieved with 60 GHz. Furthermore, both specular and diffuse powers decay faster at higher frequency, and specular power is seen to decay clearly faster than diffuse power. The XPR and large scale parameters are only weakly frequency dependent. In order to reveal any possible further differences between the studied frequencies and to allow for more conclusive analysis, more measurement and simulation data in the airport scenario is still needed.

ACKNOWLEDGMENT

The research leading to these results received funding from the European Commission H2020 programme under grant agreement in °671650 (5G mmMAGIC project), and from Nokia Bell Labs.

REFERENCES

[1] G. R. MacCartney, T. S. Rappaport, S. Sun, and S. Deng, "Indoor office wideband millimeter-wave propagation measurements and channel models at 28 and 73 GHz for ultra-dense 5G wireless networks," *IEEE Access*, vol. 3, pp. 2388–2424, 2015.

[2] mmMagic, "6-100 GHz Channel Modelling for 5G: Measurement and Modelling Plans in mmMAGIC," white paper, Feb. 2016.

[3] METIS, "Deliverable D1.1 scenarios, requirements and KPIs for 5G mobile and wireless system," METIS, Deliverable ICT-317669-METIS/D1.1, Apr. 2013. [Online]. Available: www.metis2020.com/documents/deliverables/

[4] M.-D. Kim, J. Liang, H.-K. Kwon, and J. Lee, "Directional delay spread characteristics based on indoor channel measurements at 28 GHz," in *Proc. 26th IEEE Ann. Int. Symp. Pers. Indoor Mobile Radio Commun. (PIMRC)*, Hong Kong, Aug. 30-Sept. 2 2015, pp. 403–407.

[5] R. J. Weiler, M. Peter, T. Kühne, M. Wisotzki, and W. Keusgen, "Simultaneous millimeter-wave multi-band channel sounding in an urban access scenario," in *Proc. 9th European Conf. Antennas Propag. (EuCAP)*, Lisbon, Portugal, May 13-17 2015, pp. 1–5.

[6] M. Sasaki, W. Yamada, T. Sugiyama, M. Mizoguchi, and T. Imai, "Path loss characteristics at 800 MHz to 37 GHz in urban street microcell environment," in *Proc. 9th European Conf. Antennas Propag. (EuCAP)*, Lisbon, Portugal, May 13-17 2015, pp. 1–4.

[7] K. Haneda, J. Järveläinen, A. Karttunen, M. Kyrö, and J. Putkonen, "A statistical spatio-temporal radio channel model for large indoor environments at 60 and 70 GHz," *IEEE Trans. on Antennas and Propag.*, vol. 63, no. 6, pp. 2694–2704, Jun. 2015.

[8] K. Haneda, S. L. H. Nguyen, J. Järveläinen, and J. Putkonen, "Estimating the omni-directional pathloss from directional channel sounding," in *10th European Conf. Ant. Prop. (EuCAP2016)*, Davos, Switzerland, Apr. 2016.

[9] A. Maltsev, R. Maslennikov, A. Sevastyanov, A. Khoryaev, and A. Lomayev, "Experimental investigations of 60 GHz WLAN systems in office environment," *IEEE J. Sel. Areas Commun.*, vol. 27, no. 8, pp. 1488–1499, 2009.

[10] A. Karttunen, K. Haneda, J. Järveläinen, and J. Putkonen, "Polarization characteristics of propagation paths in indoor 70 GHz channels," in *Proc. 9th European Conf. Antennas Propag. (EuCAP)*, Lisbon, Portugal, May 13-17 2015, pp. 1–4.

[11] A. F. Molisch, *Wireless Communications*, 2nd ed. New York: IEEE Press-Wiley, 2011.